ISSN (Print) 1226-1750
ISSN (Online) 2233-6656
Journal of Magnetics 25(1), 78-85 (2020) https://doi.org/10.4283/JMAG.2020.25.1.078

Detection for Position of Electrode Tip of Submerged Arc Furnaces with the Differential Magnetic Field Radiation

WeiLing Liu[1], LingZhen Yang[2], and XiaoMing Chang[3]*

[1]College of Data Science, Taiyuan University of Technology, No. 79 Yingze West Street, Taiyuan 030024, Shanxi, PR China
[2]College of Physics and Optoelectronics, Taiyuan University of Technology, No.79 Yingze West Street, Taiyuan 030024, Shanxi, PR China
[3]College of Information and Computer Science, Taiyuan University of Technology, No.79 Yingze West Street, Taiyuan 030024, Shanxi, PR China

(Received 22 January 2020, Received in final form 12 March 2020, Accepted 12 March 2020)

The differential magnetic field sensing is proposed to detect the position of the electrode tip for the smelting of the submerged arc furnace (SAF). The magnetic radiation model is established by the magnetic differences between the electrode zone and electric arc zone in the industrial field of SAF and the differential magnetic field sensing system is developed. The experiments are carried out under the environment of industrial field. When the relative distance between the two probes is appropriately set, the field test curve can accurately reflect the position of the electrode tip. Theoretical analysis and experimental results show that the difference of the front end of the system can detect the position of the electrode tip and effectively avoid saturating the system. Compared with the detection of magnetic field array sensing, the differential magnetic field detection scheme is more effective for the position information of the electrode tip and has better practical value for industrial measurement.

Keywords : submerged arc furnace, the position of electrode tip, differential magnetic field detection

1. Introduction

Submerged arc furnace (SAF) is an industrial electric furnace which can smelt ores and extract useful metals by electric arc discharge. The electric arc occurs between the furnace burden and the tip of electrodes which are the critical components that inject large current into the furnace to perform arc smelting [1]. In the process of smelting, heat distribution in the furnace and balance degree of three-phase power in the molten bath is regulated by lifting and lowering electrodes [2, 3].

The position of the electrode tip is essential for the smelting process of SAF. There are several detection methods for the position of the electrode tip as follows.

(1) Electrode weighing method. The working length of the electrode can be calculated by detecting the variables such as self-weight of the electrode [4], lifting displacement and slipping length of the electrode and so on. However, the pressure measurement exits error for the reasons that furnace burden has the support function to the electrode and the electrode mass changes slightly with a short time, and the detection error may rise due to the nonuniform wear. The pressure sensor, ultrasonic sensor and encoder used in electrode weighing method need to be installed on the hydraulic cylinder, electrode holder and large vertical cylinder of SAF. But the furnace needs to stop working in order to install the equipment, which brings a cost loss and is not conducive to the later production.

(2) Photoelectric sensing method [5, 6]. The photoelectric and position sensors have been used to design an online detection system for the relative position of electrodes. However, photoelectric sensing requires the detection system to keep the short distance with the SAF and keep working at the high temperature of SAF. The accuracy of photoelectric sensing method is low and has its limitation in practice. This method is in the stage of laboratory simulation experiment and research [6], and has not been applied to the field of SAF.

(3) Array sensing using electromagnetic method [7].

*Corresponding author: Tel: 13233697523
Fax: 0351-6014033, e-mail: 644855751@qq.com

The magnetic field array sensing method for detection of smelting in SAF is proposed [7]. However, it needs to be considered to identify the characteristics of the electrode tip accurately for the high-power and high-capacity SAF.

A differential magnetic field sensing detection scheme based on the electromagnetic principle is proposed, and the detection for the position of the electrode tip in SAF is realized. The theoretical and experimental results show that the method is effective in determining the position of the electrode tip.

The paper is organized as follows: The theoretical background of the measurement is introduced in section 2. Section 3 describes the verification of the differential magnetic field detection scheme. Thereafter analysis of field measurement results is presented in Section 4, and conclusions are given in Section 5.

2. Theory Background

2.1. Magnetic field detection methods and related issues

The hearth structure [8-10] of SAF is shown in Fig. 1.

The electric arc is generated between the electrode tip and the molten bath from Fig. 1. The molten alloys gather in the molten bath and the liquid level is the top of the molten bath surface.

The large currents flow into the furnace by the electrodes, and the circuit can be regarded as the star circuit loop and the triangle circuit loop [11, 12], and the two types of loops can be equivalently transformed in the sense of electromagnetic. Therefore, we use the triangle loop to analyze the circuit model. Based on the electromagnetism, magnetic field radiation model of SAF [13] is established as shown in Fig. 2.

In Fig. 2, I_A, I_B, and I_C are the currents of electrode A, B, and C, respectively, and I_{AC}, I_{CB}, and I_{BA} are the currents in the molten bath. Currents flow into the furnace along each electrode and form a triangle circuit loop near the liquid surface. I_{AC} is the molten bath current parallel to the x-axis at point P_1; I_C is the electrode current parallel to the z-axis at point P_2. The concepts of electrode line and perpendicular bisector are defined as shown in Fig. 3.

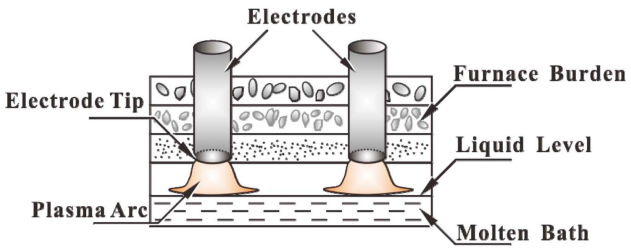

Fig. 1. (Color online) The hearth structure of SAF.

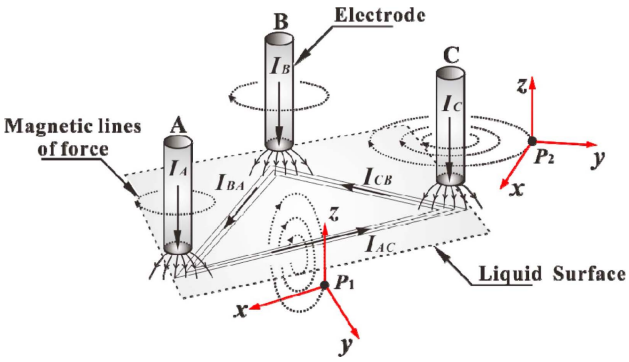

Fig. 2. (Color online) The magnetic field radiation model of SAF.

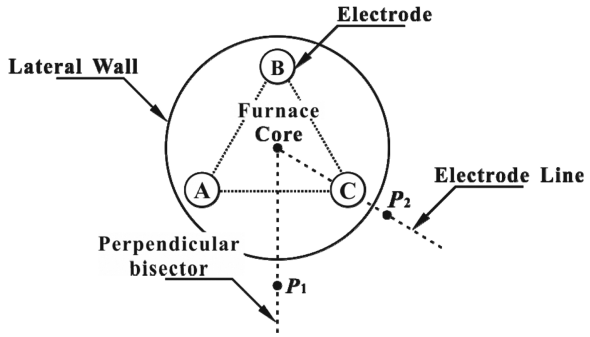

Fig. 3. The plan view of SAF.

In Fig. 3, the plan view of SAF is given. On the plane parallel to the molten bath surface, a regular triangle is generated by connecting three vertex electrodes, and the core of SAF is the center of the triangle. The line connecting the electrode and the furnace core is called electrode line. The vertical of each edge of the regular triangle is termed as perpendicular bisector. The point P_1 and P_2 is the measured origin of electrode line and perpendicular bisector, respectively. It can be seen that the perpendicular bisector is parallel to y-axis at point P_1, and electrode line is parallel to y-axis at point P_2.

The detecting system of 3D magnetic field [13] is composed of three identical subsystems, and the outputs of three dimensions along the x, y and z-axis are V_x, V_y, V_z, respectively. Take the x-direction as an example to explain the system in which the circuit is composed of probe, operational amplifier (OPA), low-pass filter (LPF), and RMS conversion circuit, and it is shown in Fig. 4.

In Fig. 4, the AC signal from the probe for the detection of the magnetic field information is translated into the effective value signal as the output signal through OPA circuit, LPF circuit and RMS conversion circuit.

The method of magnetic field array sensing detection and the detection method of 3D single point have been proposed and discussed [7]. Compared with the detection

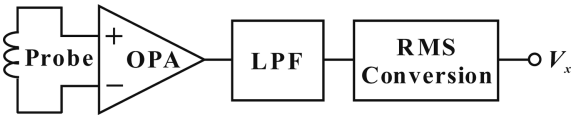

Fig. 4. The composition of magnetic field detection subsystem.

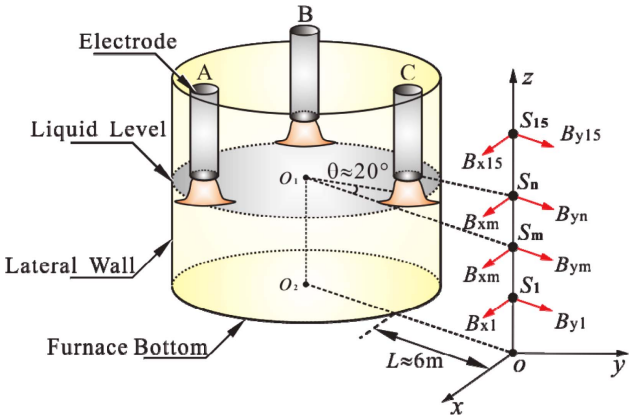

Fig. 5. (Color online) The sketch of measuring points in real industrial field.

method of 3D single point, the array sensing detection method has the higher efficiency and the superiority over real-time performance and precision. The measuring schematic diagram of the array sensing method in real industrial field is shown in Fig. 5.

In Fig. 5, the distance between the origin o and the array sensor S_1 is 10 cm, and the electrode tip can be covered by the measurement range.

The real measurements on the SAF (6300 KVA) is achieved at a metallurgical company in Yinchuan city in China. The testing result in industrial field is shown in Fig. 6.

In Fig. 6, the intersection of h~V_x curve and h~V_z curve, namely 80 cm ≤ h ≤ 100 cm, reflects the position of the

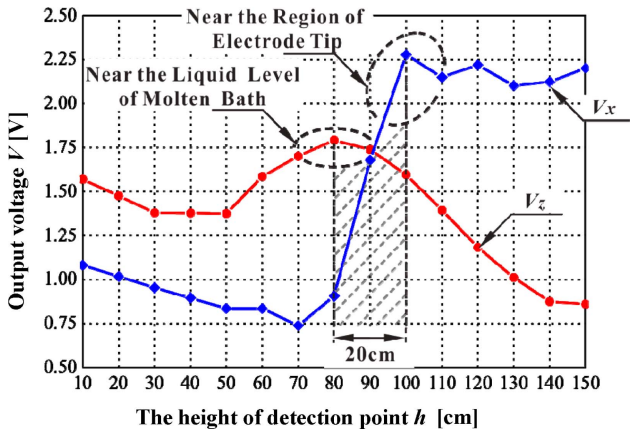

Fig. 6. (Color online) The testing results of 6300 KVA SAF.

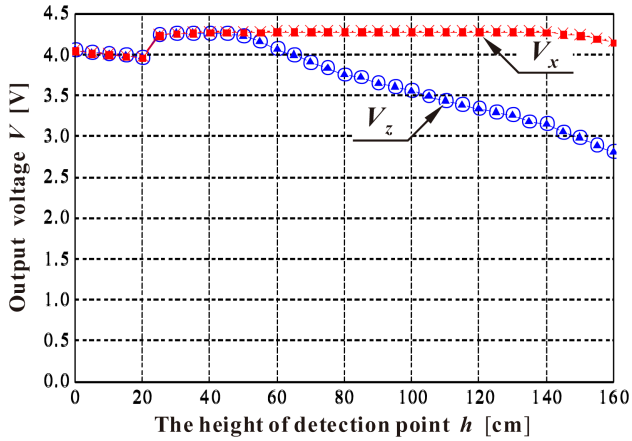

Fig. 7. (Color online) The testing results of 33000 KVA SAF.

electrode tip. It can be seen that the magnetic field array sensing method can reflect the distribution characteristics of the magnetic field of SAF and detect the position of the electrode tip.

The same array sensors were used to perform the same experiment on a high-power and high-capacity SAF (33000 KVA) at another metallurgical company in Yinchuan city in China. The results are shown in Fig. 7.

By analysis of the curve in Fig. 7, the large current of 33000 KVA SAF causes the output saturation of the magnetic field detection system. The signal of the electrode tip is weaker relative to the overall output of the system at the same time, and it is difficult to extract the information about the electrode tip. So how to achieve the position of the electrode tip has become a new problem.

2.2. Distribution characteristics of current and magnetic field near the electrode tip

2.2.1. Current distribution in electrode zone and arc zone

In order to analyze conveniently, the electrode top is assumed to be the origin o, and take p points vertically down as the test points (S_1,…, S_m,…, S_n,…, S_p), among which the point S_m is located near the electrode tip, and the point S_n is near the liquid level, $m < n < p$, and the distance between these test points and the point o is (d_1,…, d_m,…, d_n,…, d_p). The distribution model of electrode current, arc current and the current in molten liquid of SAF is shown in Fig. 8 [14, 15].

In Fig. 8 the current is uniformly distributed in the electrode above the detected point S_m in the electrode zone ($d_1 \le d_i \le d_m$). However, the randomness and non-uniformity of the arc current direction will inevitably be presented due to the change of the medium between the detected point S_m and S_n ($d_m \le d_i \le d_n$) in the arc zone [16].

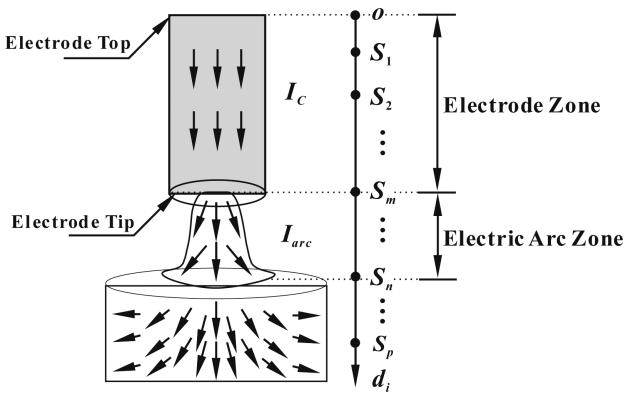

Fig. 8. The current distribution of electrode, electric arc and molten bath.

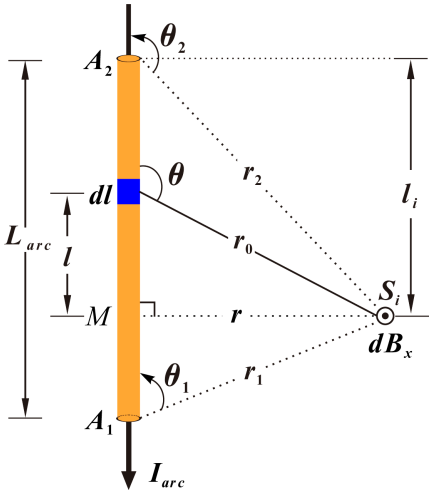

Fig. 9. (Color online) The magnetic induction intensity of the measuring point S_i in electric arc zone.

2.2.2. Magnetic field distribution in arc zone

The electric arc is equivalent to a current-carrying straight wire A_1A_2 with the finite length. The length and the average current at z-axis direction are L_{arc} and I_{arc}, respectively. The line S_iM is the vertical line of electric arc A_1A_2, and the length of S_iM is r, and r is the distance between the test point and the center of arc column, as shown in Fig. 9.

Based on the Biot-Savart law [17], the magnetic induction intensity dB which is generated by any current element Idl is all going in the same direction which is perpendicular to the surface of the paper outside and is parallel to the x-axis. Therefore, only the algebraic sum of dB_x [18] is needed to calculate the total magnetic induction intensity B_x at the test point S_i. For the finite electric arc A_1A_2, the total magnetic induction intensity B_x at the test point S_i can be described as Eq. (1).

$$B_x = \int_{A_1}^{A_2} dB_x = \frac{\mu_0}{4\pi}\int_{A_1}^{A_2} \frac{I_{arc}\, dl \sin\theta}{r_0^2} \tag{1}$$

where I_{arc} is the current of the electric arc. r_0 is the radius vector from the current element Idl to the test point S_i. r_1 is the radius vector from the starting point A_1 of the straight wire carrying current I_{arc} to the field point S_i. r_2 is the radius vector from the end point A_2 of the straight wire carrying current I_{arc} to the field point S_i. θ_1 is the angle between the radius vector r_1 and the current element located at the starting point A_1 of the straight wire. θ_2 is the angle between the radius vector r_2 and the current element located at the end point A_2 of the straight wire.

The foot of a perpendicular M is taken as the original point, and l is assumed as the distance from the current element Idl to the foot point M. It can be seen from Fig. 9:

$$\begin{cases} l = r_0\cos(\pi-\theta) = -r_0\cos\theta \\ r = r_0\sin(\pi-\theta) = r_0\sin\theta \end{cases} \tag{2}$$

in which r is the distance from the detection point S_i to the vertical line S_iM of the electrode A_1A_2.

According to Eq. (2), r_0 is eliminated, the distance l from the current element Idl to the foot point M can be expressed by the following equation:

$$l = -r\cot\theta \tag{3}$$

Take the derivative with respect to l, and then dl that is the differential calculus of l is given as Eq. (4).

$$dl = \frac{rd\theta}{\sin^2\theta} \tag{4}$$

Change the integral variable l of Eq. (4) to θ, so the total magnetic induction intensity B_x at the test point S_i is presented as Eq. (5).

$$\begin{aligned} B_x &= \frac{\mu_0}{4\pi}\int_{\theta_1}^{\theta_2} I_{arc}\frac{\sin\theta}{r}d\theta \\ &= \frac{\mu_0 I_{arc}}{4\pi r}(\cos\theta_1 - \cos\theta_2) \end{aligned} \tag{5}$$

From Fig. 9, the expressions of $\cos\theta_1$ and $\cos\theta_2$ are described in Eq. (6).

$$\begin{cases} \cos\theta_1 = \dfrac{L_{arc}-l_i}{\sqrt{(L_{arc}-l_i)^2+r^2}} \\ \cos\theta_2 = -\dfrac{l_i}{\sqrt{l_i^2+r^2}} \end{cases} \tag{6}$$

where L_{arc} is the distance between the extreme points A_1 and A_2 of the electrode; l_i is the distance between the test point S_i and the point S_m which is located at the electrode tip.

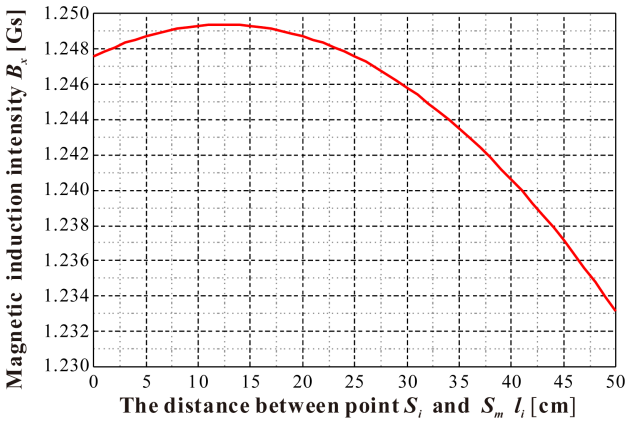

Fig. 10. (Color online) The simulation result of magnetic induction intensity in the electric arc zone.

According to Eq. (5) and Eq. (6), the total magnetic induction intensity B_x at the test point S_i is expressed by the following equation:

$$B_x \approx \frac{\mu_0 I_{arc}}{4\pi r}\left(\frac{L_{arc}-l_i}{\sqrt{(L_{arc}-l_i)^2+r^2}}+\frac{l_i}{\sqrt{l_i^2+r^2}}\right) \tag{7}$$

Because the detection point is outside of the furnace, μ_0 is equal to $4\pi\times10^{-7}$ H/m, and I_{arc} is approximately equal to 40 kA [18, 19]. Combined with the parameters of SAF in real measurements, the values of the parameter r and L_{arc} are set to $r=1$ m and $L_{arc}\approx50$ cm, respectively. According to Eq. (7), we use Maple software to carry out simulation, and the result is shown in Fig. 10.

We make the conclusions that the magnetic induction intensity B_x in the arc zone is normally distributed, and the magnetic induction intensity B_x is the maximum in the arc zone when $l_i = 12$ cm or $l_i = 13$ cm from Fig. 10.

2.2.3. Magnetic field distribution in electrode zone

Since the current is uniformly distributed in the electrode, the electrode can be regarded as a current-carrying straight wire. The magnetic field strength model in the electrode zone is similar to the detection model of the arc zone within the range above the detection point S_m ($d_1 \le d_i \le d_m$). The magnetic field strength is

$$B_x = \frac{\mu_0 I_C}{4\pi r}(\cos\theta_1 - \cos\theta_2) \tag{8}$$

The electrode length is much longer than the arc length, so when the detection point is close to the electrode, the distance r from the detection point S_i to the straight wire carrying current I_C is much less than the electrode length L_C, namely $r << L_C$, while $\theta_1 \to 0$, $\theta_2 \to \pi$. The total magnetic induction intensity B_x of the detection point S_i in the electrode zone is given in Eq. (9).

$$B_x \approx \frac{\mu_0 I_C}{2\pi r} \tag{9}$$

The strength of the electrode current I_C basically remains unchanged from Eq. (9). The magnetic field strength at the test point in the electrode zone is mainly constant, which is obviously different from the situation in the electric arc zone.

2.2.4. Simulated experiment of current direction at the electrode tip

In order to confirm the overall change trend of the magnetic induction intensity at the electrode tip, the two trends of electrode zone and electric arc zone should be taken together for qualitative analysis. The simulation experiment can prove the inference that both the current and the distribution of magnetic field are continuous.

5A current is applied to the L-type electrothermal wire

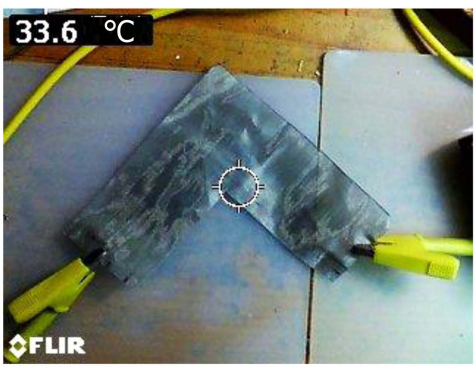

(a) The electrothermal wire mesh connected to electricity

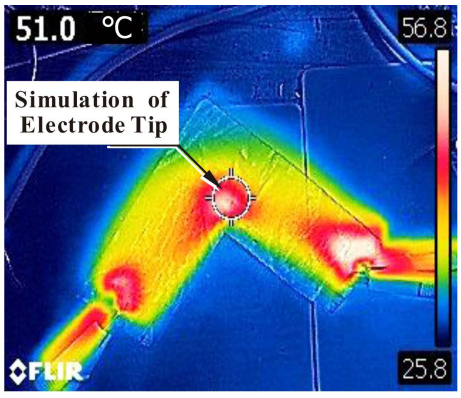

(b) The infrared imagery of the electrothermal wire mesh when electrified

Fig. 11. (Color online) The simulated experiment of electrode current direction.

mesh and the current flow direction at the corner is observed with a thermal imager as shown in Fig. 11.

The current distribution at the corner of the electro-thermal wire mesh flows to the other end mainly through the inner bending, which makes a difference on the uniformity of the current in the conductor. The change caused by the uniformity of the current inevitably leads to the change of the magnetic field vector outside, which is consistent with Fig. 10.

2.3. A differential detection scheme to obtain the position of the electrode tip

According to the changing law of arc current and the variation tendency of the magnetic field at the detection point on the electrode line, at a certain time the magnetic induction intensity distribution of the detection system on the electrode line of SAF is qualitatively described as shown in Fig. 12.

The conclusions can be obtained from Fig. 12. In the electrode zone, the output voltage V_x is mainly influenced by the electrode current I_C and remains constant within the scope of $0 \le d_i \le d_m$. Near the electrode tip the output voltage V_x changes when $d_i = d_m$. In the electric arc zone, V_x increases first and then decreases as h_i increases in the range of $d_m \le d \le d_n$

In Fig. 12, the two adjacent test points S_i and S_{i-1} are taken and the output of the detection system are V_{xi} and $V_{x(i-1)}$, respectively. The output difference at the two points S_i and S_{i-1} is set as ΔV_{xi}. The results from the field measurement of the 33000 KVA SAF are presented as Eq. (10).

$$\Delta V_{xi} = \left| V_{xi} - V_{x(i-1)} \right| \ll V_{sat} \tag{10}$$

where V_{sat} is the saturation output voltage of magnetic field detection system.

The system output voltage shown in Eq. (11) is the voltage at the front end multiplied by the gain of the system.

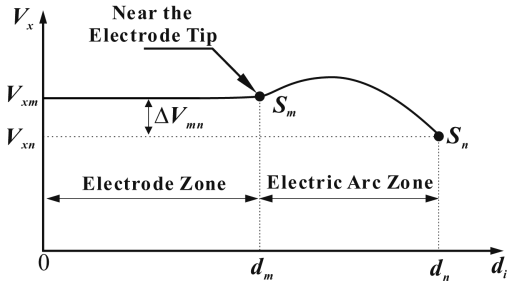

Fig. 12. The variation tendency of output voltage V_x of the system in electrode zone and electric arc zone.

$$\begin{cases} V_{xi} = u_{xi} \times G \\ V_{x(i-1)} = u_{x(i-1)} \times G \end{cases} \tag{11}$$

where u_{xi} is the voltage at the front end of the magnetic field detection system at test point S_i; G is the gain of the magnetic field detection system.

Due to the large current of 33000 KVA SAF, the output voltage V_{xi} and $V_{x(i-1)}$ of the test points S_i and S_{i-1} are close to the system saturation voltage V_{sat}. The output difference ΔV_{xi} at the two points S_i and S_{i-1} is expressed by the flowing equation:

$$\begin{aligned} \Delta V_{xi} &= \left| u_{xi} \times G - u_{x(i-1)} \times G \right| \\ &= \left| u_{xi} - u_{x(i-1)} \right| \times G \ll V_{sat} \end{aligned} \tag{12}$$

The saturation phenomenon can be avoided by making the output difference at the front of the system before the signal is amplified.

3. Verification of Differential Magnetic Field Detection Scheme

3.1. Realization of the differential magnetic field signal detection

It can be seen from Eq. (12) that before the signal is amplified, how to make the output difference between the two coils at the front of the system is the key to the problem. According to the principle of electromagnetic induction, the two coils with opposite polarity are connected in series, then the difference value between the voltages at the front of the magnetic field detection system is described as Eq. (13).

$$\Delta u_{xi} = \left| u_{xi} - u_{x(i-1)} \right| \tag{13}$$

The circuit structure of differential magnetic field signal detection system is shown in Fig. 13.

In Fig. 13, the probe is composed of two coils with opposite polarity, which detect magnetic field information at different spatial positions. The difference value between the outputs of the two coils is converted into output ΔV_{xi} by the OPA circuit and LPF circuit, and then by the TRMS conversion circuit. The expression of ΔV_{xi} is given as Eq. (14).

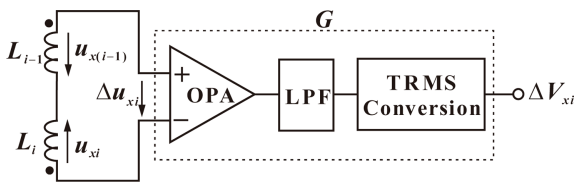

Fig. 13. The model of magnetic field sensing system based on the differential principle.

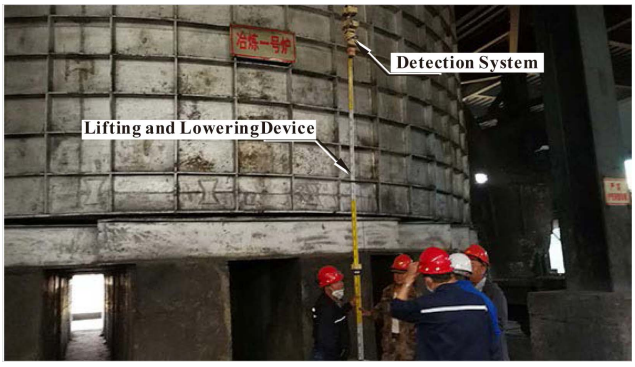

Fig. 14. (Color online) The experimental scene in industrial field.

$$\Delta V_{xi} = \Delta u_{xi} \times G \tag{14}$$

The analysis shows that the differential detection scheme doesn't saturate the system output.

3.2. Field measurement of differential detection method

We perform real measurements on the 33000 KVA SAF at a metallurgical company of Yinchuan city in China. Through the multiple experiments, we choose the test site at the electrode line, and the test site is about 1 m away from the lateral wall. The experimental scene in industrial field is shown in Fig. 14.

The height of the furnace in Fig. 14 is 5.6 m. Starting from the top of the electrode, several points are sampled along the *z*-axis with a step length of 40 cm, and each point is collected 6 times to take its average value. The test results are shown in Fig. 15.

After several experiments, the distance between the two coils of the designed system is set as 40 cm.

4. Analysis of Field Measurement Results

In the measurement, only the V_{xi} component of the

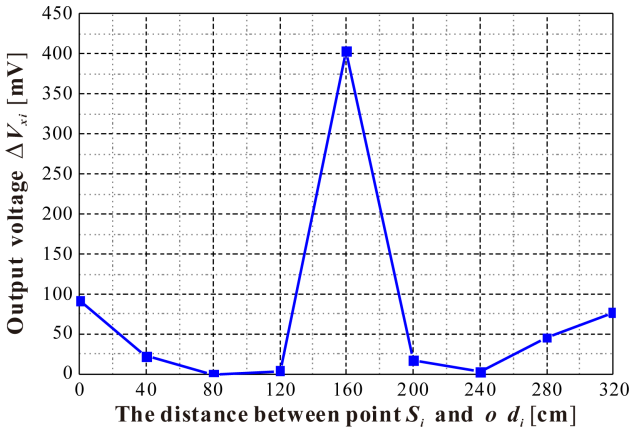

Fig. 15. (Color online) The testing results in industrial field.

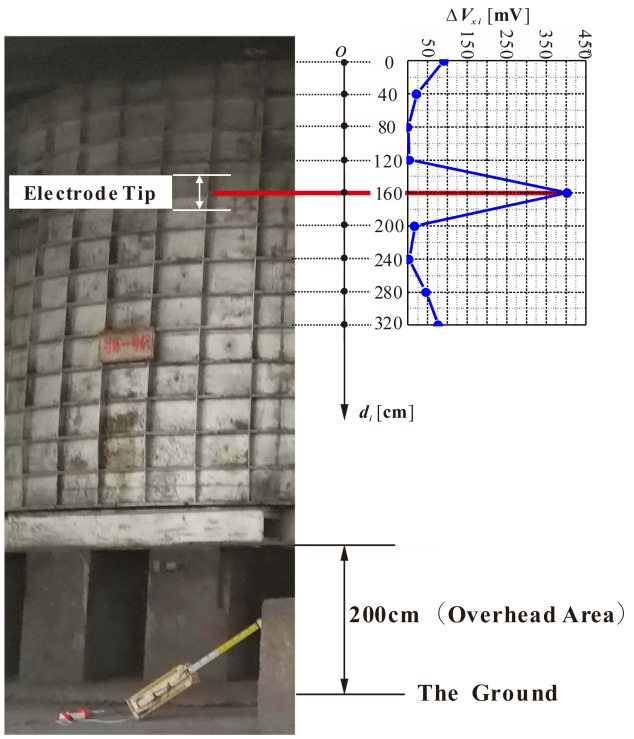

Fig. 16. (Color online) The analysis on testing results.

electrode current is obtained at the position of the system, so only the $d_i \sim \Delta V_{xi}$ curve is analyzed. The furnace is corresponding to the test curve, as shown in Fig. 16.

From Fig. 16 it can be found that:

(1) When $0 \le d_i \le 120$ cm, the differential output ΔV_{xi} of the system is close to zero. It can be inferred that the segment lies above the electrode tip, which is consistent with the actual situation.

(2) The peak point appears at the test point $d_i = 160$ cm. Since the distance between the two coils of the system is 40 cm, we can conclude that the region of the electrode tip is in the range of 140 cm $\le d_i \le$ 180 cm, which is in accordance with the field situation of SAF.

(3) The interval of $d_i \ge 200$ cm is the molten pool area. The dielectric of the molten pool is, by and large almost uniform, and the molten pool current is relatively dispersed, so the system output is relatively low and is close to zero.

5. Conclusions

In this paper, a differential magnetic field detection method is proposed to achieve the position of the electrode tip of SAF. Theoretical analysis and experimental results show that the distribution characteristics of the magnetic field of SAF can be reflected and the position of the electrode tip can be obtained by the differential magnetic field detection. Compared with the magnetic field detec-

tion, the differential magnetic field detection can extract the characteristics of the electrode tip and improves the measurement accuracy.

Acknowledgements

This research has been supported by National Natural Science Foundation of China under Grant (61975141 and 61575137).

References

[1] M. Moghadasian and E. Alenasser, J. Electromagn. Anal. Appl. **3**, 47 (2011).
[2] A. C. Mulholland, P. J. Breretonstiles, and C. J. Hockaday, J. S. Afr. I Min Metall. **109**, 601 (2009).
[3] N. N. Zhang, Z. J. Wang, and D. J. Zhang, IEEE. Comput. Mechatr. Contr. Electr. Eng. **3**, 108 (2010).
[4] C. X. Tang, C. H. Yang, P.Li, and X. X. Lei, J. Changsha. Social. Work. Col. **20**, 123 (2013).
[5] Y. Bai, Q. Wang, F. R. Meng, and H. Y. Wang, J. ChangChun. Univ. T, **33**, 383 (2012).
[6] Z. H. An, Ms. D. Thesis, Changchun University of Technology, China (2010).
[7] W. L. Liu, X. H. Han, L. Z. Yang, and X. M. Chang, J. Magn. **21**, 322 (2016).
[8] S. J. Chu, S. L. Zeng, and Z. C. Huang, Ferro-Alloys. **2**, 13 (2009).
[9] S. J. Chu, X. E. Bao, and Z. S. Li, Ferro-Alloys. **3**, 22 (2013).
[10] A. S. Hauksdottir,T. Soderstrom, Y. P. Thorfinnsson, and A. Gestsson, IEEE.T. Contr. Syst. T. **3**, 377 (1996).
[11] Q. H. Xiao, Ferro-Alloys. **1**, 11 (1982).
[12] N. S. Zhang, Ferro-Alloys. **6**, 1 (1986).
[13] W. L. Liu and X. M. Chang, J. Magn. **21**, 204 (2016).
[14] Z. K. Wang, T. W. Li, and B. K. Li, J. Mater. Metall. **12**, 177 (2013).
[15] J. Alexis, M. Ramirez, G. Trapaga, and P. Jonsson, ISIJ. International. **40**, 1089 (2000).
[16] Y. A. Tesfahunegn, T. Magnusson, M. Tangstad, and G. Saevarsdottir, J. S. Afr. I. Min. Metall. **118**, 595 (2018).
[17] Q. G. Reynolds and R. T. Jones, Miner. Eng. **19**, 325 (2006).
[18] O. J. P. Gonzalez, M. A. R. Argaez, and A. N. Conejo, ISIJ. International. **50**, 1 (2010).
[19] F. Martell, M. Ramirez, A. Llamas, and O. Micheloud, ISIJ. International. **53**, 743 (2013).